J Mater Sci (2008) 43:3135–3143
DOI 10.1007/s10853-008-2502-8

Structural and chemical properties of nanocrystalline $La_{0.5}Sr_{0.5}CoO_{3-\delta}$ layers on yttria-stabilized zirconia analyzed by transmission electron microscopy

L. Dieterle · D. Bach · R. Schneider · H. Störmer · D. Gerthsen · U. Guntow · E. Ivers-Tiffée · A. Weber · C. Peters · H. Yokokawa

Received: 21 December 2007 / Accepted: 24 January 2008 / Published online: 28 February 2008

Abstract Nanocrystalline $La_{1-x}Sr_xCoO_{3-\delta}$ (LSC) thin films with a nominal Sr content $x = 0.5$ were deposited on 3.5 mol% yttria-stabilized zirconia (YSZ) substrates by a low-temperature sol–gel process followed by a rapid thermal annealing procedure at temperatures up to 900 °C. The structural and chemical stability of the as-prepared nanocrystalline LSC and demixing effects within the thin film or at the LSC/YSZ interface were studied after long-time exposure at temperatures between 700 °C and 1,000 °C. The grain size and surface topography were analyzed by scanning electron microscopy. Transmission electron microscopy combined with selected-area electron diffraction, energy-dispersive X-ray spectrometry, and electron-spectroscopic imaging was applied for the investigation of the microstructure and the analysis of the local chemical composition and element distribution on the nanoscale. Chemical potential calculations, which were performed to assess the decomposition of LSC/YSZ as a function of temperature, show good agreement with the experimental results.

L. Dieterle (✉) · D. Bach · R. Schneider · H. Störmer · D. Gerthsen
Laboratorium für Elektronenmikroskopie and DFG Center for Functional Nanostructures (CFN), Universität Karlsruhe, Karlsruhe 76128, Germany
e-mail: dieterle@lem.uni-karlsruhe.de

U. Guntow
Fraunhofer-Institut für Silicatforschung, Neunerplatz 2, Wurzburg 97082, Germany

E. Ivers-Tiffée · A. Weber · C. Peters
Institut für Werkstoffe der Elektrotechnik and CFN, Universität Karlsruhe, Karlsruhe 76128, Germany

H. Yokokawa
National Institute of Advanced Industrial Science and Technology (AIST), Energy Technology Research Institute, AIST Central 5, Higashi 1-1-1, Tsukuba 305-8565, Japan

Introduction

Mixed ionic-electronic conductors (MIECs) are promising cathode materials for solid oxide fuel cells (SOFCs). In contrast to cathodes with negligible ionic conductivity, an improved performance of SOFCs can be achieved by MIECs because the oxygen reduction reaction is not confined to the triple-phase boundary between electrolyte, cathode, and gaseous environment. Among the class of MIECs $La_{1-x}Sr_xCoO_{3-\delta}$ (LSC) is characterized by a high electronic and ionic conductivity and high activity for oxygen reduction [1, 2]. A nanocrystalline and nanoporous microstructure is expected as an effective approach to minimize the cathodic polarization losses for intermediate-temperature SOFC [3] due to the increased surface area and high density of grain boundaries which are expected to lead to enhanced oxygen diffusion [4]. The fabrication of nanocrystalline LSC or LSCF thin films on electrolyte substrates has already been demonstrated by effective techniques such as pulsed laser deposition [5–10], DC and RF sputtering [11, 12], spray pyrolysis [13], and sol–gel deposition [14–18].

In this work the chemical and structural stabilities of LSC thin films on polycrystalline YSZ substrates produced by a low-temperature sol–gel technique were investigated, which appears to be a promising route to custom film thickness in the range of 50–500 nm as well as grain size and porosity on the nm scale. The nominal composition

$La_{0.5}Sr_{0.5}CoO_{3-\delta}$ was chosen because of its high electronic conductivity [1] and excellent electrocatalytic properties [19], with a potential for a low cathodic polarization resistance [3]. Polycrystalline 3.5 mol% yttria-stabilized zirconia (YSZ) was introduced as substrate material to evaluate the chemical stability of nanocrystalline thin films deposited on state-of-the art electrolyte materials in a temperature range for intermediate-temperature SOFCs ($500 < T < 700$ °C) as well as high-temperature SOFC (>800 °C) [20–23]. The LSC/YSZ samples were subjected to annealing treatments at 700, 800, 900, and 1,000 °C for 8 h each.

It is well known from substantial experimental and theoretical analyses that perovskite-type cathodes of the composition $(La,Sr)(Co,M_t)O_3$ (M_t: transition metal: Mn, Fe, etc.) react with zirconia-based electrolyte materials resulting in the formation of insulating reaction products like $SrZrO_3$ and/or $La_2Zr_2O_7$ which can drastically decrease the performance of a SOFC cathode [10, 20–25]. On the other hand nanoscaled LSC thin film cathodes on YSZ are expected to be applicable at low-operating temperatures (<600 °C) [26] which can be explained by slow kinetics of the formation of secondary phases at the LSC/YSZ-interface. However, the decomposition of nanocrystalline LSC on YSZ, which is initiated by the SZO formation, has not been studied with respect to the spatial distribution and compositional (in)homogeneity of the remaining LSC grains as well as spatial distribution of secondary cobalt oxide phases. Only averaged compositions are typically given in previous work, e.g. Sase et al. [10]. We also address the possible formation of superstructures in LSC. Superstructure reflections were found previously in selected-area electron diffraction pattern by transmission electron microscopy which are attributed either to oxygen vacancy ordering [27, 28], cation, or combined cation/oxygen-vacancy ordering [29–31].

In the present study the microstructure and spatial distribution of reaction products and secondary phases in nanoscaled LSC thin film cathodes were studied by scanning and transmission electron microscopy combined with different analytical techniques. To support the experimental findings and to provide a thorough understanding for the formation of reaction products and secondary phases thermodynamic calculations were performed.

Experimental

Sample fabrication

Nanocrystalline LSC cathode layers with a nominal composition of $La_{0.5}Sr_{0.5}CoO_{3-\delta}$ were prepared by a sol–gel process on 3.5 mol% YSZ substrates. In more detail, acetates of lanthanum, strontium, and cobalt were mixed with the desired stoichiometry with propionic acid and propionic acid anhydride as solvent. Subsequently, all volatile components are removed from the reaction mixture by rotational evaporation at reduced pressure. The obtained dry precursor powder is dissolved on demand. 13 wt.% of precursor powder was dissolved in a mixture of propanoic and nonanoic acid with a ratio of 1:9 serving as a ready-for-use sol. Three thin LSC layers were deposited successively on a YSZ substrate by dripping the sol on the substrate and dispersing it uniformly by spin coating with 2,000 r/min for 60 s. The samples were then exposed to a rapid thermal annealing procedure (RTA) consisting of three successive steps at furnace temperatures of 170 °C for 15 min, 700 °C for 15 min, and 900 °C for 15 min. Heating up and cooling down took place within seconds, because the samples were exposed to the maximum furnace temperature and back to room temperature immediately after 15 min of annealing time. Multiple sample series with a variation in organic solvent compositions were fabricated. The series with appropriate structural quality with respect to density of cracks was evaluated as a mixture of propionic and nonanoic acid with a ratio of 1:9. Subsequent to the RTA annealing treatment described above, the samples were subjected to a long-time thermal treatment at temperatures of 700, 800, 900, and 1,000 °C for 8 h to study chemical and structural changes of the nanocrystalline LSC and the interface reactions between LSC and YSZ.

Electron microscopy

The surface topography of the samples was studied by scanning electron microscopy (SEM) using a ZEISS Supra VP with a field-emission gun. Based on the SEM results, samples were selected for transmission electron microscopy (TEM). Selected-area electron diffraction (SAED), conventional and high-resolution TEM (CTEM/HRTEM) imaging were performed with a 200-keV Philips CM200 FEG/ST equipped with a field-emission gun. The local chemical composition of the samples was analyzed by energy-dispersive X-ray spectrometry (EDXS) by means of a Noran Vantage system with a Ge detector. Electron-spectroscopic imaging (ESI) was performed with a 200-kV LEO 922 Omega transmission electron microscope with an in-column Omega energy filter. Based on electron-spectroscopic images, the element distribution was revealed by means of the three-window technique [32].

Two different techniques were applied for TEM sample preparation. Plan-view samples were prepared conventionally by grinding, polishing, and Ar-ion milling. Cross-section samples with a homogeneous thickness of about 100 nm were prepared by focused ion beam (FIB) milling

using the H-bar technique [33] by the following preparation steps. Two sample pieces with an area of 1 mm × 2 mm were glued together with the thin film LSC layers oriented against each other. Top and bottom sides of this sandwich were polished to an overall thickness of about 40 μm. The front face which is used for the ion milling was polished, too. Subsequently, the sandwich is mounted into a halved TEM aperture grid. In a combined SEM/FIB system (ZEISS EsB 1540 Crossbeam), a focused Ga-ion beam is used to cut out two 40 μm long cuboids perpendicular to the glue gap until a thin membrane remains which is stabilized by the surrounding thicker material. A thin line of Pt was deposited previously by ion-beam-induced deposition on the glue gap to protect the front face of the milled membrane against the tail of the Ga^+ beam.

Results

Grain size analysis and surface topography

Figure 1 shows SEM micrographs of the samples which were annealed at 700, 800, 900, and 1,000 °C for 8 h. The mean grain size increases with the annealing temperature from 54 ± 25 nm as prepared after RTA to 100 ± 40 nm at 700 °C and 390 ± 140 nm at 1,000 °C (cf. Fig. 2). For comparison, the average grain size of 54 ± 25 nm after RTA is also included in Fig. 1. The grain-size evaluation was carried out by estimating the mean grain diameter from a circle being equivalent to the grain area. For this purpose about 200 grains of each sample were analyzed excluding secondary phases and pores.

Besides the typical LSC grains, grains with different morphology marked by arrows in Fig. 1a and Fig. 1d can be detected after an exposure time of 8 h at temperatures ≥700 °C. Rectangular grains (see black arrows in Fig. 1a) occur in the sample annealed at 700 °C which are not observed at higher temperatures. Samples tempered at 1,000 °C show grains (Fig. 1d, marked by white arrows) without pronounced crystal facets. Analyzing the composition of these grains by EDXS in the scanning electron microscope suggests a cobalt-rich phase. Due to the large penetration depth of electrons with an energy of 10 keV, quantitative chemical analyses of individual grains were not possible. Skeleton-shaped grains could be observed on the surface of the Co-rich grains (Fig. 1d, marked by black arrows). In addition to the samples annealed at the lowest and highest temperature, one sample without supplemental annealing was selected for a detailed TEM study. These specimens are denoted as LSC-RTA, LSC700, and LSC1000 in the following.

Microstructure and local chemical composition

Figure 3 displays two representative overview bright-field TEM images of LSC700 and LSC1000 plan-view samples. An increase of the mean grain size as a function of temperature can be observed which is consistent with the SEM results. The bright-dark contrast variations within grains (cf. Fig. 2b) are ascribed to local sample bending. Grains with distinct bright contrast (marked by arrows in Fig. 2b) could be identified as cobalt oxide by EDXS. The composition of ten individual LSC grains was analyzed in thin regions of the plan-view samples where the YSZ substrate was removed. A significant Sr deficiency was detected in both samples with Sr concentrations between 0.38 and 0.44 in LSC700 and a significantly more pronounced chemical inhomogeneity in LSC1000 with Sr concentrations between 0.14 and 0.44.

SAED patterns of LSC1000 were taken at low temperatures using a liquid-nitrogen cooled double-tilt holder to analyze the LSC structure and the possible formation of superstructures. Liquid-nitrogen cooling appeared appropriate because the observation of diffraction patterns at room temperature yields superstructure reflections with increasing intensity during extended observation duration. It is well known that LSC occurs either in the cubic or rhombohedrally distorted perovskite structure (according to [34], space group R-3c, with lattice parameters $a = 5.4256$ Å and $c = 13.240$ Å, Wyckoff positions: 6a La/Sr, 6b Co, 18e (0.546, 0, 0.25) O). The latter occurs at lower Sr concentrations. For room temperature the respective phase transition takes place at $x \sim 0.5$ [1, 35]. In addition, the lattice parameter increases with the Sr concentration from 0.3827 nm for $x = 0$ to 0.3843 nm for $x = 0.8$ [34]. Due to the detected Sr deficiency we expect rhombohedrally distorted perovskite structure. However, for simplified visualization, cubic indexing (marked by a subscripted c) is used in the following for pseudocubic directions. Figure 4a, b shows representative SAED patterns of LSC1000 along the $[100]_c$ and $[110]_c$ zone axes (ZA) of grains with a chemical composition of $La_{0.86}Sr_{0.14}CoO_{3-\delta}$ and $La_{0.81}Sr_{0.18}CoO_{3-\delta}$. The corresponding kinematical simulations of the diffraction patterns by the JEMS software package [36] are displayed in Fig. 4c, d which are based on structure data of Hagerty et al. [34] for the rhombohedral unit cell. Neither ordering on the A-sublattice (La/Sr) nor on the anion sublattice (oxygen ions/oxygen vacancies) was assumed. Sharp reflections of the type $(2n - 1)$ $\{1/2\ 1/2\ 1/2\}_c$ $(n = 0, 1, 2,...)$ are observed along the $[110]_c$ zone axis (marked by circles in Fig. 4b) which are kinematically forbidden in the rhombohedral unit cell. Dynamical electron diffraction is responsible for these reflections because their intensity weakens strongly under off-axis diffraction conditions, which excludes the

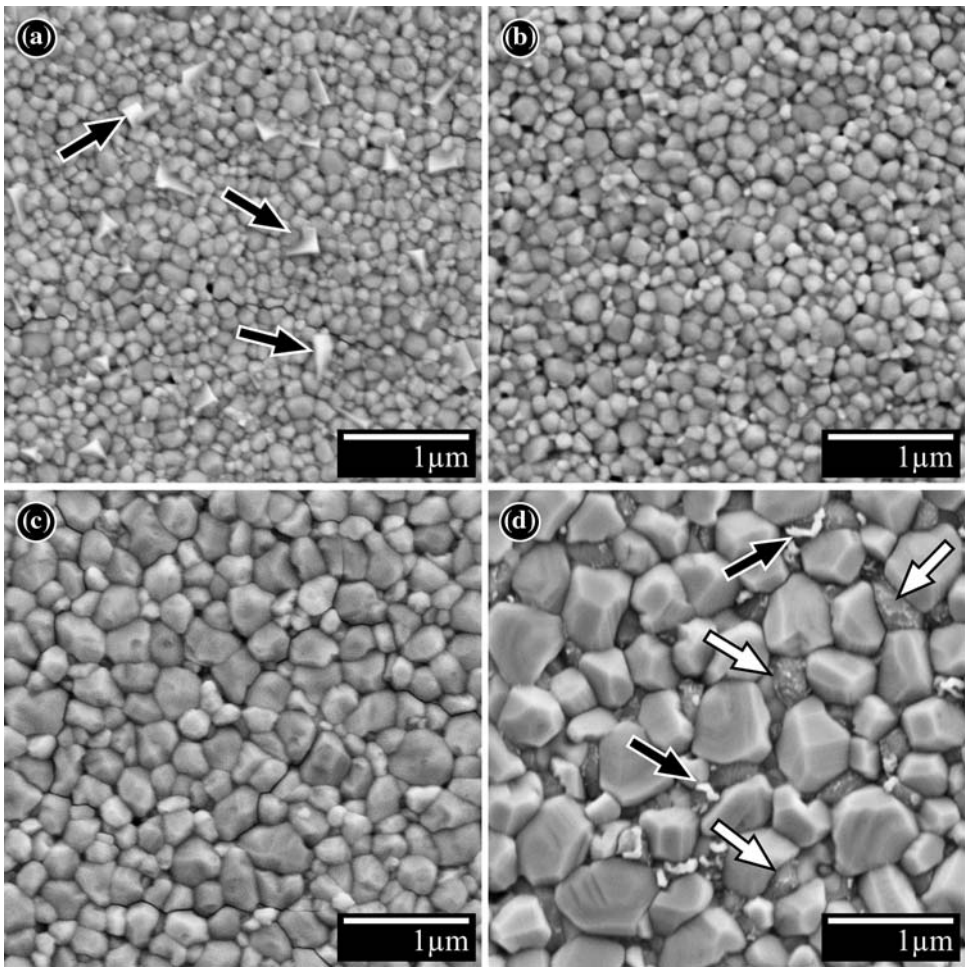

Fig. 1 SEM images of the samples annealed at (**a**) 700 °C, (**b**) 800 °C, (**c**) 900 °C, and (**d**) 1,000 °C for 8 h

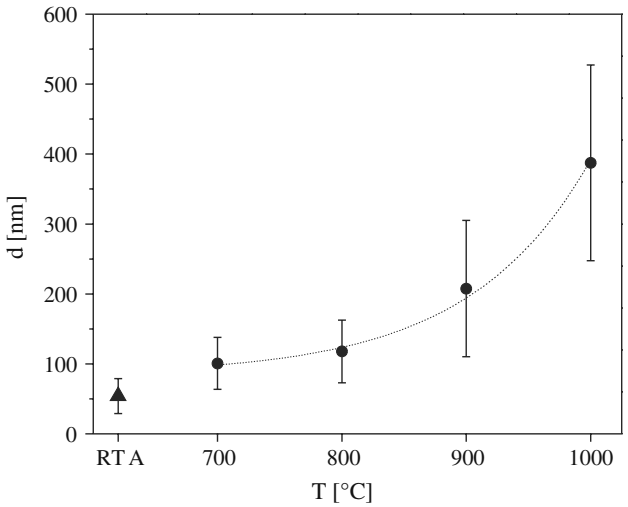

Fig. 2 Mean diameter d of LSC grains versus annealing temperature T after 8 h. The average grain size after RTA (triangular symbol) is included for comparison

presence of a superstructure. SAED patterns show diffuse $\{1/2\ 0\ 0\}_c$ or $\{1/3\ 0\ 0\}_c$ superstructure reflections even in a liquid-nitrogen cooled holder under prolonged electron-beam irradiation. These reflections correspond to a cubic lattice parameter of 7.6 Å and 11.4 Å, respectively.

SAED patterns of individual grains in LSC700 could not be obtained due to the small grain sizes around 100 nm (the smallest available SAED aperture corresponds to a size of 220 nm). For a better comparison of the two samples, Debye diffraction patterns were taken from plan-view samples of LSC700 and LSC1000 (Fig. 5). The samples were thinned from the backside to remove the YSZ substrate and reaction phases at the interface. Due to larger grain sizes in LSC1000 (Fig. 5b), the density of reflections on the diffraction rings is reduced compared to LSC700 (Fig. 5a). In addition to LSC, reflection rings are found in both samples (see magnified insets 1 and 2 in Fig. 6) which can be assigned to Co_3O_4 with a spinel structure (space group Fd-3m, $a = 8.084$ Å, Wyckoff positions: 8a Co, 16d Co and 32e (0.392, 0.392, 0.392) O) [37]. Another secondary phase with large unshaped grains is present in LSC1000 according to the SEM micrograph, Fig. 1d. TEM/EDXS analyses of these grains yield an atomic cation ratio of Co:Sr:La = 99:0:1, indicating also a cobalt oxide phase. The distinction between CoO, CoO_2, and Co_3O_4 was

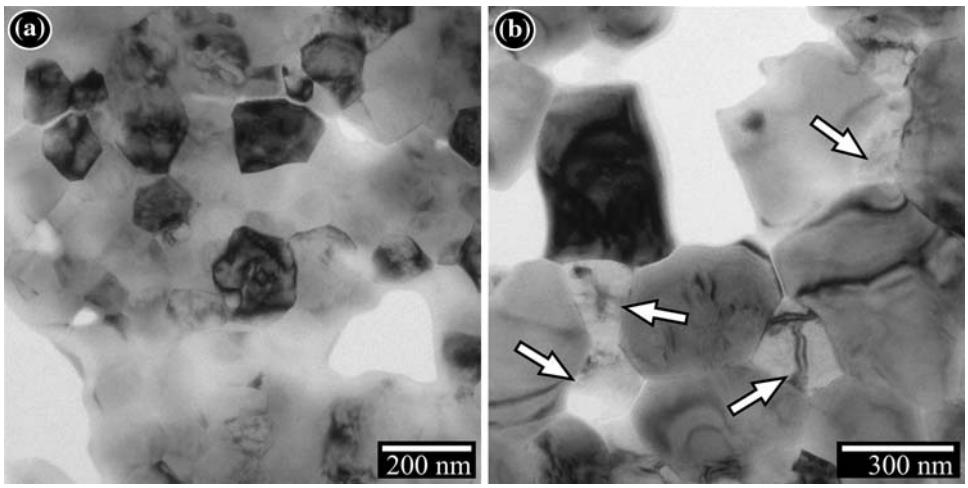

Fig. 3 TEM bright-field images of (**a**) LSC700 and (**b**) LSC1000 plan-view samples

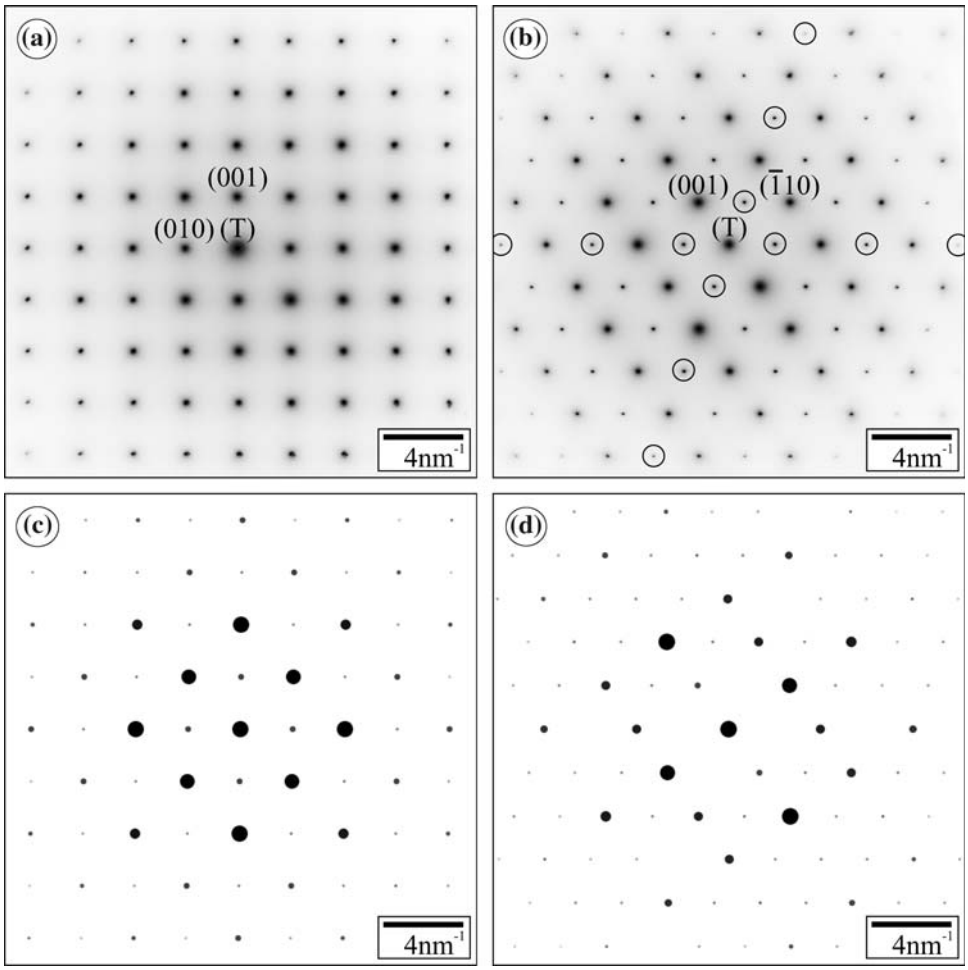

Fig. 4 Experimental SAED patterns of sample LSC1000 along the (**a**) $[100]_c$ and (**b**) $[110]_c$ ZA; and (**c**, **d**) corresponding kinematical simulations

accomplished by SAED. Symmetry and lattice distances of the SAED pattern correspond to the cubic face-centered structure of cobalt(II) oxide (CoO) (space group Fm-3m, $a = 4.2518$ Å, Wyckoff positions: 4a Co, 4b O) [38].

Cross-section samples were studied to analyze the microstructure and distribution of the different phases as a function of the distance from the interface. Figure 6a, b displays zero-loss-filtered TEM images of both samples

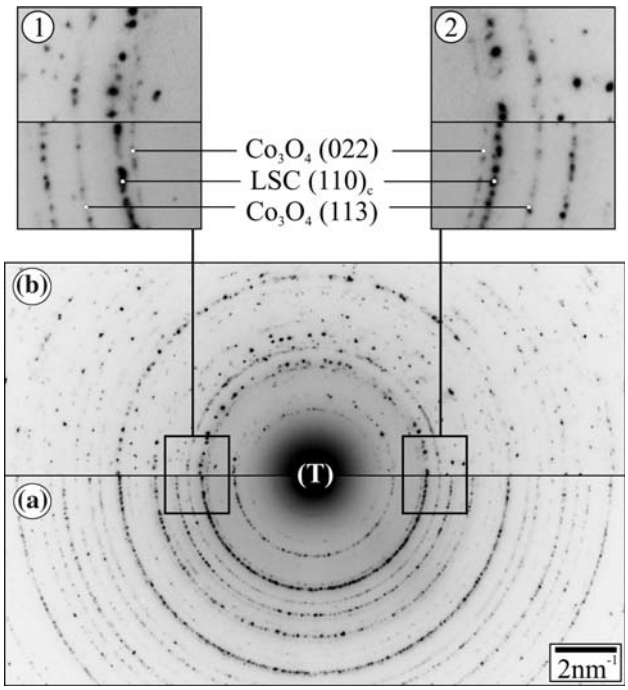

Fig. 5 Debye diffraction patterns of (**a**) LSC700 and (**b**) LSC1000

which show layers with a thickness of about 240 nm on top of the YSZ substrate. An interfacial layer marked by white dashed lines in Fig. 6a, b is observed in both samples with an average thickness of 42 ± 5 nm in LSC700 (Fig. 6a) and a larger thickness of 130 ± 20 nm in LSC1000 (Fig. 6b).

Electron-spectroscopic images were recorded to obtain a comprehensive overview of the element distribution in the LSC/YSZ interface region. The La–$N_{4,5}$ edge (edge onset at an energy loss $\Delta E = 90$ eV) was used for imaging the La distribution (bright regions in Fig. 6c, d). LSC700 (Fig. 6c) exhibits an inhomogeneous La distribution. Even grains without La were detected. The latter grains are partly located within the La-rich region and also at the substrate/layer interface. In LSC1000 (Fig. 6d), La is confined completely to the surface region. Only a small amount of La is located in subjacent grains. In contrast, Sr mapped with the Sr–$L_{2,3}$ edge at $\Delta E = 1{,}940$ eV is depleted at the surface and enriched at the interface. This effect is more pronounced in LSC1000 (Fig. 6f) than in LSC700 (Fig. 6e). The Sr-enriched layer corresponds to the interfacial layer in Fig. 6a, b. SAED patterns of larger grains of LSC1000 were taken. The symmetry of the SAED patterns and the evaluated lattice-plane distances correspond well to the perovskite structure of the $SrZrO_3$ (SZO) phase.

The Co distribution imaged with the Co–$L_{2,3}$ edge ($\Delta E = 779$ eV) visualizes that the grains depleted in Sr

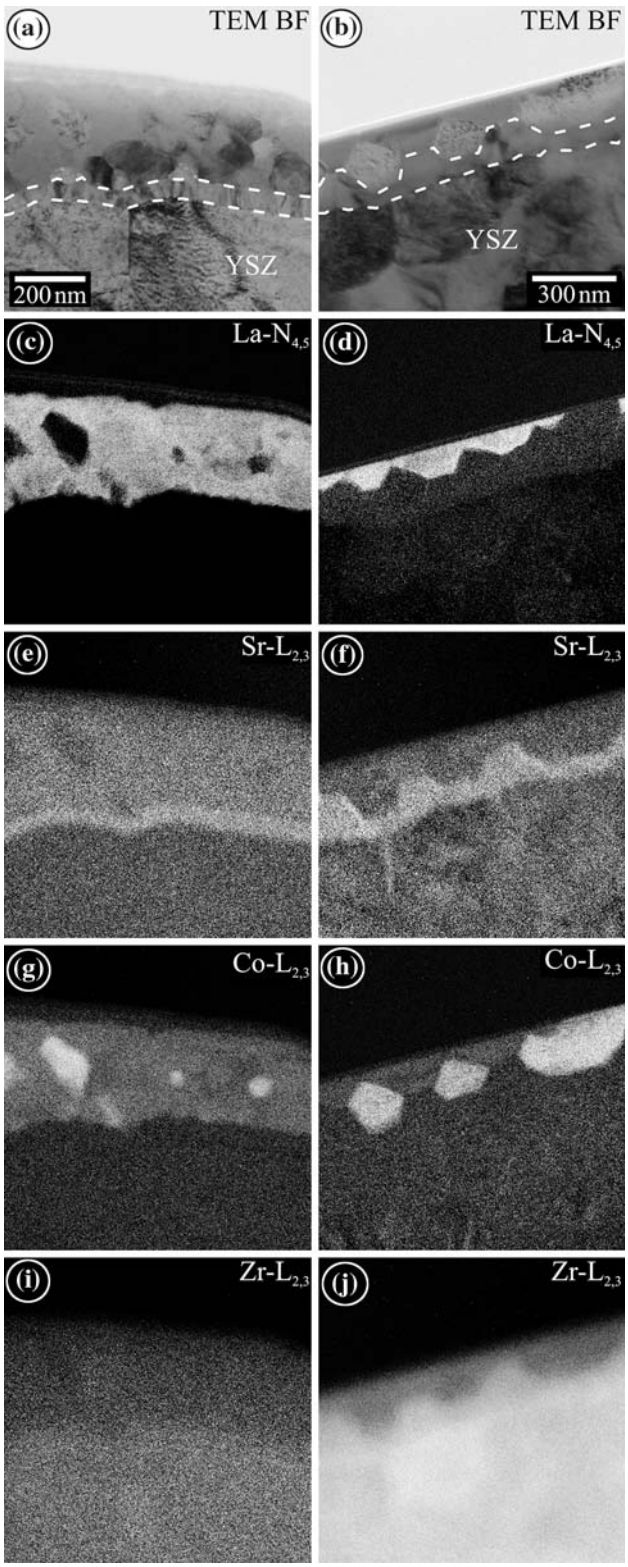

Fig. 6 Zero-loss-filtered TEM images of (**a**) LSC700 and (**b**) LSC1000 and ESI micrographs of both samples of the (**c**, **d**) La, (**e**, **f**) Sr, (**g**, **h**) Co and (**i**, **j**) Zr distributions

and La are cobalt oxides (as also verified by EDXS and SAED). These regions correspond to the grains with bright and speckled contrast in Fig. 6a, b.

In case of LSC700 (Fig. 6g) the Co_3O_4 grains are embedded in the LSC layer. In LSC1000 (Fig. 6h), the CoO grains lie between the LSC and the Sr-rich reaction layer. As expected for the SZO reaction layers, the Zr distribution (imaged with the Zr–$L_{2,3}$ edge at $\Delta E = 2{,}222$ eV) shows a higher Zr content exactly in those regions where an enrichment of Sr is found. This effect is more pronounced in LSC1000 (Fig. 6j) than in LSC700 (Fig. 6i). The Zr signal, which is visible in the LSC layer, can be ascribed to Zr redeposition during FIB milling. Owing to a large sample drift particularly caused by high electron-irradiation doses, the lateral resolution of the maps for elements with high energy-loss edges like Zr and Sr is deteriorated. The element distribution obtained by ESI could be confirmed by corresponding EDXS maps.

Cross-section images of LSC-RTA (not shown here) demonstrate that the SZO phase is already formed during the RTA process at the LSC/YSZ interface with an average thickness of 16 ± 3 nm. In addition to reflections of the rhombohedrally distorted LSC structure, Debye diffraction patterns contain reflections of the Co_3O_4 phase which is formed likewise during the RTA process.

Thermodynamic calculations

To contribute to the understanding of the formation of the different observed phases and the decomposition of the perovskite phase, thermodynamic calculations were performed with the MALT software package [39] to assess the stability of LSC in contact with ZrO_2. Details of the method are outlined in [40]. The necessary thermodynamic data for the present calculations were taken mainly from the thermodynamic database MALT which is based on the NBS chemical thermodynamic data [41] combined with available heat capacities; except for (La, Sr)$CoO_{3-\delta}$, numerical values are given in [42–46]. The data for the $SrCoO_{3-\delta}$ component in LSC was determined so as to reproduce the oxygen nonstoichiometry in $SrCoO_{3-\delta}$ [47] and the phase relation in the La–Sr–Co–O system [48].

The calculations were performed for $La_{1-x}Sr_xCoO_3$ with an initial Sr content $x = 0.5$ and a ZrO_2 activity of 1 at 1 atm and an oxygen partial pressure of 0.21 atm. Figure 7 shows the computed phase diagram of the O–Co–Zr–La–Sr system. In the diagram four regions are visible. At high temperatures (Region 1) the perovskite phase is not stable and will decompose into $La_2Zr_2O_7$ (LZO), SZO, ZrO_2, and CoO. At lower temperatures the stability of the perovskite phase is restricted to high La/Sr-ratios (Region 3), whereas at the nominal composition investigated in this work (La/Sr = 1) the perovskite is partly decomposed resulting

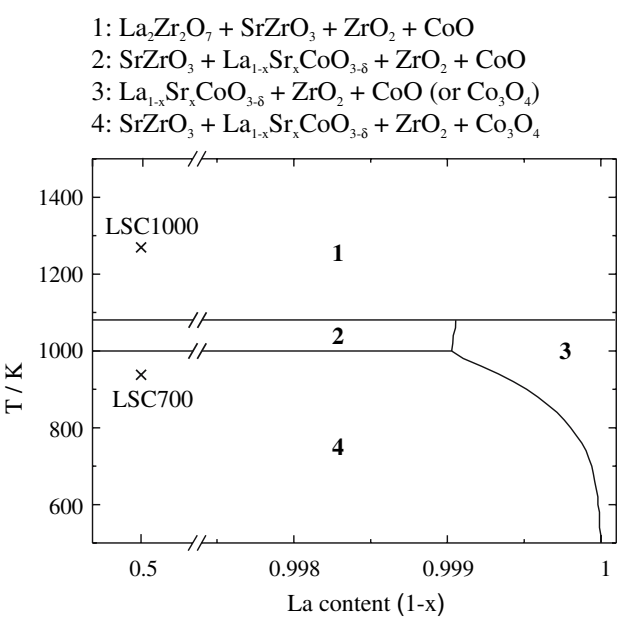

Fig. 7 Phase diagram of the O–Co–Zr–La–Sr system at $p = 1$ atm, p(O2) = 0.21, log a(ZrO2(c)) = 0

in the formation of SZO and CoO (Region 2), respectively, Co_3O_4 (Region 4). According to these results the LSC perovskite layer should react completely with the zirconia substrate to SZO and LZO at 1,000 °C, whereas at 700 °C only SZO should be formed as a reaction product. The remaining cobalt oxide should be CoO at 1,000 °C, respectively, Co_3O_4 at 700 °C.

Discussion

The evaluation of the average grain sizes presented in Fig. 2 shows that grain growth is significant at 700 °C/8 h compared to the grain sizes immediately after RTA but remains almost unchanged between 700 °C and 800 °C. In this temperature range, fully crystallized layers are obtained with well-preserved nanocrystalline structure and average grain sizes of 100 and 120 nm. At higher temperatures, the grain diameter roughly doubles every 100 K and an average grain diameter of 390 nm is reached at 1,000 °C. The increase of the average grain size as a function of the temperature can be fitted by an exponential function.

Due to the Sr deficiency, the LSC occurs in the rhombohedral instead of the cubic perovskite structure [1]. SAED analyses show that the presence of a superstructure can be excluded despite the observation of reflections of the type $\{1/2\ 1/2\ 1/2\}_c$ because these reflections are excited dynamically in zone-axis SAED patterns. The lack of a superstructure is in contradiction to the findings of several other groups that reported the formation of superstructures

in LSC by ordering of oxygen vacancies [24, 28] which is well known in anion-deficient perovskites [49–51]. Wang et al. [29, 30] explained the superstructure first as cation ordering. Later they described it as combined cation/anion-vacancy ordering [31] for a Sr/La ratio of approximately 1. Likewise Stemmer et al. [28] could not completely exclude this combined model. In the present work superstructures could not be observed in diffraction patterns which were obtained in a liquid nitrogen-cooled sample holder, which prevents or at least delays beam-induced ordering processes. Additional diffuse $\{1/2\ 0\ 0\}_c$ or $\{1/3\ 0\ 0\}_c$ superstructure reflections, which occur with increasing intensity during extended electron-beam exposure at room temperature and for longer observation periods at liquid-nitrogen temperature, must be assigned to the effect of electron-beam-induced ordering.

The formation of SZO is observed as a reaction product in the interface region between the YSZ substrate and LSC already after RTA and, with increasing volume fraction, after annealing at 700 °C and 1,000 °C (Fig. 6). This is expected according to previous studies, e.g. by Ivers-Tiffée et al. [22] and Sase et al. [10], who found a Sr- and Zr-rich interlayer at the YSZ/LSC interface. After a long-term heat treatment (158 days) at 700 °C Sase et al. [10] roughly estimated the thickness of this layer to about 150 nm by means of secondary ion mass spectrometry. The thickness of the SZO layer in our sample LSC700 is significantly smaller (42 nm ± 5 nm) after annealing at 700 °C which can be partly attributed to the comparably short (8 h) annealing time. After annealing at 1,000 °C, larger SZO grains are found with leads to the confinement of LSC grains to the surface region of the sol–gel layer (Fig. 6d, f).

Grains of two different cobalt oxide phases are embedded in the layers. Debye electron diffraction (Fig. 5) reveals the presence of Co_3O_4 in LSC700 and LSC1000 which appears as rectangular-shaped grains on the sample surface in corresponding SEM micrographs (Fig. 1a). The Co_3O_4 grains exhibit the same morphology as Co_3O_4 grains in a cobalt oxide film deposited by Burriel et al. [52] using pulsed-injection metal-organic chemical vapor deposition. This phase was also found by Kweon et al. [17] in a sol–gel derived LSC-thin film. Another cobalt oxide, namely CoO, was detected in LSC1000.

An interesting point to note is the morphology of the reaction products. In samples without nanocrystalline structure, SZO and CoO_x phases tend to be arranged in a band-like morphology. In contrast, CoO_x phases form as isolated particles in our nanocrystalline samples. The lack of continuous CoO_x bands will enhance SZO formation because Sr does not need to diffuse through the CoO_x phase. Advanced decomposition of the LSC perovskite phase in LSC1000 leads to a pronounced spatial separation of the different phases with a La-rich LSC perovskite phase segregated at the surface, a continuous SZO reaction layer in the LSC/YSZ interface region, and large volume fraction of isolated cobalt oxide grains in between.

According to the thermodynamic calculations at 700 °C the LSC perovskite phase remains partly stable. The formation of SZO and Co_3O_4 is accompanied by a Sr depletion of the perovskite phase—in accordance with the experimentally observed phases in LSC700. In the LSC1000 sample we find a Sr-deficient LSC perovskite phase instead of LZO and Co_3O_4 in addition to CoO. The presence of the Co_3O_4 phase can be attributed to the cooling down procedure after the annealing process at 1,000 °C. The lack of the LZO phase in LSC1000 can be understood as follows. The high activity of Sr in contact with ZrO_2 suggests that the SZO phase is formed first which leads to a Sr depletion of LSC phase. However, the formation of the LZO can be only expected at extremely low Sr concentrations. Other inhibiting factors with respect to LZO formation may be the reduction of the ZrO_2 activity after SZO formation and the spatial separation between LSC and ZrO_2 by the SZO reaction layer in our diffusion-couple samples.

Conclusions

A sol–gel processing technique was applied successfully to deposit nanocrystalline $La_{1-x}Sr_xCoO_{3-\delta}$ thin films with a nominal Sr content $x = 0.5$ on polycrystalline YSZ electrolyte substrates, which have the potential to be applied as a functional cathode layer in low- and intermediate-temperature SOFCs. After deposition and rapid thermal annealing (RTA), the samples were subjected to an 8-h annealing treatment at temperatures of 700, 800, 900, and 1,000 °C. The average grain size of about 50 nm after RTA increases to 100 nm after an additional thermal treatment at 700 °C/8 h and remains in the 100-nm range up to 800 °C/8 h.

Selected-area electron diffraction studies in a transmission electron microscope using a liquid-nitrogen cooled sample holder exclude the formation of superstructures for the given LSC compositions. Superstructure reflections are only observed as an electron-beam- induced effect. This even applies if a liquid-nitrogen cooled sample holder is used after extended illumination periods.

TEM investigations of cross-section samples show the formation of $SrZrO_3$ in the interface region between LSC and YSZ even after RTA treatment at a maximum temperature of 900 °C and 15 min, which increases significantly in thickness at temperatures of 700 °C and an exposure time of 8 h. Due to the formation of the $SrZrO_3$ reaction layer deviations from the desired stoichiometry of $La_{0.5}Sr_{0.5}CoO_{3-\delta}$ with a strong Sr depletion are detected. LSC grains in the sample annealed at 1,000 °C are

characterized by highly inhomogeneous Sr concentrations between 0.14 and 0.44. As a consequence, a La-saturated perovskite with rhombohedrally distorted instead of a cubic crystal structure is observed. Due to the resulting Co supersaturation of the LSC, cobalt oxide phases are precipitated. Co_3O_4 is observed after annealing at 700 °C for 8 h in accordance with predictions based on calculated chemical potential diagrams. The same holds for the CoO phase observed after annealing at 1,000 °C. The additional Co_3O_4 phase observed must be attributed to the cooling down procedure. This sample is characterized by a pronounced spatial separation of the different phases which is taken as an indication for the trend toward complete decomposition of the initial LSC perovskite in nanocrystalline layers at high temperature. As a consequence, LSC thin films deposited by a low-temperature sol–gel process on a state-of-the art YSZ substrate, which exhibit a promising grain size distribution on the nm scale after RTA thermal treatment at 700 °C for 15 min, already shows a deterioration due to interface reactions. Testing of electrochemical performance and more intense investigations on stability in the temperature regime between 450 °C and 650 °C are necessary to answer the question, if the combination LSC/YSZ is applicable for low-temperature operation as apparent in micro SOFCs.

Acknowledgements This work has been performed within the project D5 of the DFG Research Center for Functional Nanostructures (CFN) and within a joint DFG-NSF project. It has been further supported by a grant from the Ministry of Science, Research and the Arts of Baden-Württemberg (Az: 7713.14–300).

References

1. Petrov AN, Kononchuk OF, Andreev AV et al (1995) Solid State Ionics 80:189
2. Ralph JM, Schoeler AC, Kumpelt M (2001) J Mater Sci 36:1161
3. Ivers-Tiffée E, Weber A, Herbstritt D (2001) J Eur Ceram Soc 21:1805
4. Tuller HL (2000) Solid State Ionics 131:143
5. Chen X, Wu NJ, Ritums DJ et al (1999) Thin Solid Films 342:61
6. Baumann FS, Fleig J, Konuma M et al (2005) J Electrochem Soc 152:2074
7. Baumann FS, Fleig J, Habermeier H-U et al (2006) Solid State Ionics 177:1071
8. Koep E, Jin C, Haluska M et al (2006) J Power Sources 161:250
9. Imanishi N, Sumiya Y, Yoshimura K et al Solid State Ionics 177:2165
10. Sase M, Ueno D, Yashiro K et al (2005) J Phys Chem Solids 66:343
11. Klenov DO, Donner W, Chen L et al (2003) J Mater Res 18:188
12. Bieberle-Hütter A, Tuller HL (2006) J Electroceram 16:151
13. Beckel D, Dubach A, Studart AR et al (2006) J Electroceram 16:221
14. Kim BJ, Lee J, Yoo JB (1999) Thin Solid Films 341:13
15. Pagnaer J, Hardy A, Mondelaers D et al (2005) Mater Sci Eng B 118:79
16. Zergioti I, de Laat AWM, Guntow U et al (1999) Appl Phys A 69:433
17. Kweon HJ, Kuk S-T, Park H-B et al (1996) J Mater Sci Lett 15:428
18. Hwang HJ, Moon J, Awano M et al (2000) J Am Ceram Soc 83:2852
19. De Souza RA, Kilner JA (1998) Solid State Ionics 106:175
20. Chen CC, Nasrallah MM, Anderson HU (1993) In: Proceedings of the 3rd International Symposium on SOFC, The Electrochemical Society, Pennington, NJ
21. Yamamoto O, Takeda Y, Kanno R et al (1987) Solid State Ionics 22:241
22. Ivers-Tiffée E, Schießl M, Oel HJ et al (1993) In: Singhal SC, Iwahara H (eds) Solid oxide fuel cells III, The electrochemical society proceedings series, Pennington, NJ
23. Yokokawa H, Sakai N, Kawada T et al (1991) J Electrochem Soc 138:2719
24. Tu HY, Takeda Y, Imanishi N et al (1999) Solid State Ionics 117:277
25. Petric A, Huang P, Tietz F (2000) Solid State Ionics 135:719
26. Beckel D, Bieberle-Hütter A, Harvey A et al (2007) J Power Sources 173:325
27. Klenov DO, Donner W, Foran B et al (2003) Appl Phys Lett 82:3427
28. Stemmer S, Jacobson AJ, Chen X et al (2001) J Appl Phys 90:3319
29. Wang ZL, Zhang J (1995) Philos Mag A 72:1513
30. Wang ZL, Zhang J (1996) Phys Rev B 54:1153
31. Wang ZL, Yin JS (1998) Philos Mag B 77:49
32. Reimer L (1993) Transmission electron microscopy. Physics of image formation and microanalysis (series in optical sciences), Springer-Verlag Berlin and Heidelberg GmbH & Co. K
33. Li J, Malis T, Dione S (2006) Mater Charact 57:64
34. Haggerty RP, Seshadri R (2004) J Phys Condens Matter 16:6477
35. Mineshige A, Inaba M, Yao T et al (1996) J Solid State Chem 121:423
36. Stadelmann P (2003) Microsc Microanal 9:60
37. Smith WL, Hobson AD (1973) Acta Crystallogr B 29:362
38. Taylor D (1984) Trans J Br Ceram Soc 83:5
39. MALT for Windows, see http://www.kagaku.com/malt/index.html
40. Yokokawa H, Sakai N, Kawada T et al (1992) Solid State Ionics 52:43
41. Wagman DD, Evans WH, Parker VB et al (1982) J Phys Chem Ref Data 11(2):392
42. Yokokawa H, Sakai N, Kawada T et al (1991) J Electrochem Soc 139(9):2719 and references quoted therein
43. Yokokawa H, Sakai N, Kawada T et al (1989) Denki Kagaku 57:821
44. Yokokawa H, Sakai N, Kawada T et al (1989) Denki Kagaku 57:829
45. Yokokawa H, Sakai N, Kawada T et al (1990) Denki Kagaku 58:161
46. Yokokawa H, Sakai N, Kawada T et al (1990) Denki Kagaku 58:489
47. Vashook VV, Zinkevich MV, Ullmann H et al (1997) Solid State Ionics 99:23
48. Cherepanov VA, Gavrilova LY, Barkhatova LY et al (1998) Ionics 4:309
49. Rao CNR, Gopalakrishnan J, Vidyasagar K (1984) Indian J Chem A 23:265
50. Hadermann J, Van Tendeloo G, Abakumov AM (2005) Acta Crystallogr A 61:77
51. Wang YG, Steinsvik S, Høier R et al (1995) J Mater Sci Lett 14:1027
52. Burriel M, Garcia G, Santiso J et al (2005) Thin Solid Films 473:98